LAWRENCE
LIVERMORE
NATIONAL
LABORATORY

UCRL-JRNL-207051

Controlled and Spontaneous Magnetic Field Generation in a Gun-Driven Spheromak

S. Woodruff, B. I. Cohen, E. B. Hooper, H. S. McLean, B. W. Stallard, D. N. Hill, C. T. Holcomb, C. Romero-Talamas, R. D. Wood, G. Cone, C. R. Sovinec

October 5, 2004

Physics of Plasmas

Controlled and Spontaneous Magnetic Field Generation in a Gun-Driven Spheromak

S. Woodruff, B. I. Cohen, E. B. Hooper, H. S. Mclean, B. W. Stallard, D. N. Hill, C. T. Holcomb, C. Romero-Talamas[†], R. D. Wood, G. Cone[❀], C. R. Sovinec[❀]

Lawrence Livermore National Laboratory, Livermore, CA 94550, USA
[†] *California Institute of Technology, Pasadena, CA*
[❀] *University of Wisconsin, Madison, WS*

Abstract. In the Sustained Spheromak Physics Experiment, SSPX, progress has been made in understanding the mechanisms that generate fields by helicity injection. SSPX injects helicity (linked magnetic flux) from 1-m diameter magnetized coaxial electrodes into a flux-conserving confinement region. Control of magnetic fluctuations ($\delta B/B \sim 1\%$ on the midplane edge) yields T_e profiles peaked at > 200eV. Trends indicate a limiting beta ($ß_e \sim 4\text{-}6\%$), and so we have been motivated to increase T_e by operating with stronger magnetic field. Two new operating modes are observed to increase the magnetic field: (A) Operation with constant current and spontaneous gun voltage fluctuations. In this case, the gun is operated continuously at the threshold for ejection of plasma from the gun: stored magnetic energy of the spheromak increases gradually with $\delta B/B \sim 2\%$ and large voltage fluctuations ($\delta V \sim 1kV$), giving a 50% increase in current amplification, I_{tor}/I_{gun}. (B) Operation with controlled current pulses. In this case, spheromak magnetic energy increases in a stepwise fashion by pulsing the gun, giving the highest magnetic fields observed for SSPX (~0.7T along the geometric axis). By increasing the time between pulses, a quasi-steady sustainment is produced (with periodic good confinement), comparing well with resistive MHD simulations. In each case, the processes that transport the helicity into the spheromak are inductive and exhibit a scaling of field with current that exceeds those previously obtained. We use our newly found scaling to suggest how to achieve higher temperatures with a series of pulses.

PACS numbers: 52.55 Hc, 52.35 Py, 52.30 Bt

For submission to Physics of Plasmas

I.1 Introduction

SSPX was designed to explore the physics of confinement and magnetic field generation in a spheromak. Although magnetic field generation has been studied for some time [1], it remains a fruitful area of research. The original spheromak formation scheme is attributed to Alfvén [2], and Lindberg was the first to observe flux amplification to result from an MHD kink [3]. By use of a magnetized coaxial gun, Turner *et al* demonstrated fast formation ($\tau_{form} \sim \tau_{Alfven}$) [4], and Jarboe *et al* showed slow formation [5]. Later, spheromak magnetic fields were generated by induction [6]. Recently, two spheromaks generated by two *separate guns* have been merged to form a single spheromak [7-9]. In another scheme, multiple current sheets are naturally expelled from a *single gun* and sustain the configuration [10]. The n=1 mode that results from a kink instability of the open flux was directly associated with current drive and field build-up before in experiment, labeled the 'dough-hook' [11] and seen in 3D MHD simulations [12]. Magnetic field generation processes in spheromaks are thought to be similar to those that form galactic magnetic fields [13], and some evidence exists for the magneto-hydrodynamic dynamo [14], thought to be an important process in the generation of astrophysical magnetic fields.

Confinement improvements in SSPX give peak T_e>200eV and core electron thermal diffusivities of $\chi_e \sim 10 m^2/s$ (previously $T_e \sim 120eV$ and $\chi_e \sim 50 m^2/s$ were reported [15]). There is evidence for island formation, indicative of toroidal surfaces, and most SSPX temperature data is bounded by a $\beta_e \sim 5\%$ [16]. Given a limiting beta (not necessarily a fundamental beta-limit), an increase of temperature is obtained by increasing the magnetic field strength ($T \sim \beta B^2$), which motivates the work presented here.

In SSPX, formation with a wide variety of initial conditions gives rise to the same linear scaling of the edge poloidal magnetic field with the injected current observed as a $B_p \sim 0.0065 I_{gun}$ [17] (much the same scaling as observed in SPHEX of $B_p \sim 0.0075 I_{gun}$ [18]). This scaling is produced during the period that the n=1 mode is present, caused by the dough-hook seen in all electrostatically-driven spheromaks. Further, when a strong electrostatic driving field is used in MHD simulations of either gun geometries or simple cylinders, a strong current-driven *n*=1 instability excited on open field lines of a plasma pinch configuration is generally seen [12][21]. It has been found for these simulations that the peak field that can be obtained also scales as a function of the gun voltage and Lundquist number (hence, also the gun current).

Here we report two new methods of magnetic field generation with reference both to SSPX experimental data and results from resistive MHD simulations in both cylindrical and more SSPX-like geometries *that exceed this linear scaling*. While the emphasis has been to understand the processes by which helicity is injected into a spheromak, another equally important end is to enhance performance by pushing towards higher field-strengths and higher temperatures. Towards this end an empirically derived scaling model [22] is presented that details means for accessing these interesting regimes.

The text is structured as follows. Section II entails a description of the experiment and of the simulation tools used here. Section III contains an analytic model based on the

inductive nature of the gun impedance during helicity injection [25]. In Section IV, new results related to the two new operating modes are presented. Section V presents a discussion of the implications of these results for the scaling to a high temperature spheromak. Section VI contains the conclusions.

II Experiment and Simulation Tools

SSPX is a coaxial-gun-driven spheromak, similar in design to the version of CTX [23] that obtained a transient 400eV electron temperature in decay. SSPX is larger in volume by a factor of eight: it has a 1m-diameter gun of equal radius to the flux conserver (in CTX, the diameter was 40cm). Nine independently programmable field coils generate the vacuum field (see Figure 1 and [15]). In this text, reference is made to a 10-point-profile Thomson scattering diagnostic, two-chord CO_2 interferometer, fast CCD imaging camera, and edge magnetic probes. Base pressures as low as 10^{-9} Torr have been achieved by baking, helium shot conditioning, glow discharge cleaning and Ti gettering, giving the burn-through of most impurities and low radiated power ($<P_{gun}/10$). The circuit that drives SSPX is shown in Figure 2: a 0.5MJ LRC circuit for the formation pulse, and 1.5MJ pulse-forming network (PFN) that can deliver constant current pulse of 200kA for around 2ms. Typical operating parameters are shown in Table 1. The circuit impedance exceeds that of the spheromak several-fold, which means that the circuit acts as a *current source*. The voltage drop across the electrodes is measured with a voltage divider mounted on the gun.

The NIMROD three-dimensional resistive-MHD code [19][20] is used here as a primary tool for understanding magnetic field generation in the spheromak. The simulation domains are assumed to be bounded with perfect conductors so that magnetic field components normal to the boundaries and electric fields parallel to the boundaries vanish except for time-independent, applied background vacuum magnetic fields. The insulating gap required for applying DC voltage is modeled by specifying a tangential electric field along the outboard bounding wall in cylindrical-geometry computations and along the upstream end of the domain in gun-geometry computations. SSPX simulations employed geometries with aspect ratios (vertical height over radius) in the range of 1 to 1.5 (SSPX is near unity in aspect ratio), major radius 0.5 to 1 m (SSPX has 0.5 m major radius), maximum magnetic fields 1 to 2 T, plasma mass densities 10^4 to 10^5 larger than in SSPX to reduce the disparity in Alfvén and resistive times, i.e., to artificially reduce the magnetic Lundquist number which is above $S\sim10^5$ in hot SSPX discharges (T_e>100eV) to a more manageable $10^3<S<10^4$ in the simulations (where we use the major radius as the characteristic length scale in the definitions of the Alfvén and resistive times). In most of these simulations, fixed constants have been assumed for the values of the electrical resistivities and thermal conductivities.

Time histories of the global parameters in the experiment (such as spheromak helicity content and field energy) are inferred by fitting equilibria generated by the CORSICA [24] code to the injected current and edge magnetic field measured in the poloidal plane. The current profile is characterized by the ratio of current to field, $\lambda = \mu_0 \mathbf{J}.\mathbf{B}/B^2$, as is customary in predominately force-free plasmas. In the fits used here, the λ-profile is modeled inside the separatrix as $\lambda = \lambda_{edge}\left(1+\alpha\overline{\psi}^n\right)/\left(1+\alpha\right)$ where $\overline{\psi}$ is a normalized flux,

varying from 0 on the magnetic axis to 1 on the separatrix, α is a fitting parameter, and $\lambda_{edge} = \lambda_{gun} = \lambda$ on the open field lines outside of the separatrix. $\lambda_{gun} = \mu_0 I_{gun}/\psi_{gun}$, where I_{gun} and ψ_{gun} are the gun current and flux. The gun voltage is V_{gun}.

III Helicity injection by inductive processes

Spheromak magnetic field generation is described with the use of 'magnetic helicity': this is a measure of the linkage of the magnetic flux, is additive, and is conserved globally in instances where magnetic energy is not (e.g. in reconnections) [25]. The helicity injection rate of the gun-driven spheromak is usually expressed in terms of the gun voltage and the flux linking two coaxial electrodes: $\dot{K} = 2V_{gun}\psi_{gun}$, and the spheromak global helicity evolution is expressed as:

$$K(t) = \exp\left(\int_0^t \frac{-dt}{\tau_K}\right)\int_0^t 2V_{gun}(t')\psi_{gun}(t')\exp\left(\int_0^{t'} \frac{dt''}{\tau_K}\right)dt' \qquad (1)$$

For time-scales short compared with the helicity dissipation time, τ_K ($t/\tau_K << 1$) the integral can be simplified to:

$$K(t) = \int_0^t 2V_{gun}(t)\psi_{gun}(t)dt \qquad (2)$$

In order to understand what it means to 'inject helicity', it has been useful to determine which processes dominate V_{gun} and to control these processes in the experiment. We have considered the following contributing factors to the gun voltage:

$$V_{gun}(t) = V_{sheath}(t) + V_{edge}(t) + \frac{d}{dt}(L(t)I_{gun}(t)) + \delta V_{gun}(t) + \Delta V_{gun}(t) \qquad (3)$$

where V_{gun} is that voltage measured at the gun, V_{sheath} is a cathode sheath drop, V_{edge} is the resistive drop in the cold edge plasma and $\delta V_{gun} + \Delta V_{gun}$ are terms related to anomalous resistive processes [26]. All of the terms except the $d/dt(LI_{gun})$ inductive term are due to processes that dissipate helicity (sheaths, resistive edge, etc). The thesis of this paper is that the main contribution to the useful helicity injection rate for discrete, controllable events originates with the $d/dt(LI_{gun})$ term, for which we can assume that the gun-flux injector flux ψ_{gun} is invariant (see discussion). We can define the effective helicity injection rate in terms of the inductive plasma processes as follows:

$$K_{eff}(t) = \int_0^t 2\dot{L}(t)I\psi_{gun}(t)dt + \int_0^t 2\dot{I}(t)L\psi_{gun}(t)dt \qquad (4)$$

$$\frac{dK_{eff}}{dt} = 2\dot{L}I\psi_{gun} + 2\dot{I}L\psi_{gun} \qquad (5)$$

In Eq. (5) and below, L and $\dot{L}$ are redefined as appropriate time averages, consistent with the experimental observation that in many experimental discharges one or the other is nearly constant for extended times.

To illustrate the inductive generation of helicity, the two main sources of impedance understood to dominate during helicity injection are shown in Figure 3. For clarity, these are labeled Type I processes and Type II processes. The processes have analogues. **Type I processes** exhibit geometric changes like the plasma arcades of a Jacobs ladder: an area change results in a large dL/dt term and so the first term in the right side of Eq. (5) is dominant. **Type II processes** occur like ramping current up in a fixed geometry, like a circuit inductor which gives rise to a dI/dt term, making the second term in the right side of Eq. (5) dominant. Therefore, to add helicity to a spheromak it is necessary to choose processes that have the characteristic of inductive impedance. Two processes that give an inductive impedance are described in the following analytic examples.

Analytic expression of Type I process. Consider the instance that a single current sheet is expelled from the gun. If this occurs on a time-scale that is short compared with the rate of change of gun current then I_{gun}~const. By ignoring resistive impedance (assuming that this will be small in comparison with the inductive component) the gun voltage is $V_{gun} = I_{gun}\dot{L}$, and the effective helicity-injection-rate is $\dot{K}_{eff} = 2\psi_{gun} I_{gun}\dot{L}$.

This injection rate can be rewritten in terms of the gun current alone by considering the following. In order for the sheet to be released from the gun, a pressure balance in the gun must be met in which the axial constraining force of the radial vacuum field is balanced by the JxB force acting on the current sheet. The only control parameter that is varied during this ejection process is the gun current, and so the pressure balance is often expressed in terms of a threshold current, I_{thresh}. Equating magnetic pressures, the equality $B_\theta = B_p$ is obtained for the expulsion of a current sheet. Expressing the gun flux in terms of the gun current by using a sharp boundary model (see Appendix 2) one obtains an expression for the gun flux at the time of ejection in terms of the gun current and the gun geometry:

$$\psi_{gun} = \mu_0 I_{thresh}\Delta/4 \qquad (6)$$

Where the inter-electrode gap width is Δ, and the radius is R. Finally, the helicity injection rate can be written in terms of the threshold current, geometry and rate of change of inductance due to the length expansion of the current sheet:

$$\dot{K}_{eff} = \mu_0 I_{thresh}^2 \dot{L}\Delta/2 \qquad (7)$$

The helicity content of the spheromak can be determined by use of Eq. 7 and knowledge of the inductance of the current sheet expanding from the gun approximated as a coaxial

cylinder: $L = (\mu_0/2\pi) l_{sheet} \log(r_2/r_1)$, where r_2 and r_1 are the outer and inner electrode radii respectively, l_{sheet} is the length of the sheet (including both gun and flux-conserver regions), giving L~100nH. By combining the two expressions for L and $\dot{K}$, a geometrical relationship for the magnetic helicity introduced with each current sheet is obtained. Integrating with respect to time, the helicity of the spheromak can be predicted from knowledge of the threshold current alone: $K = 9 \times 10^{-15} I_{thresh}^2 Wb^2$.

Analytic expression of Type II process. The inductance of a screw-pinch can be expressed by considering the limiting case where the column and return current form a coaxial section of fixed geometry (see Appendix 3). Before the onset of asymmetry and before a spheromak is established (for which $\psi_{pol} \sim \psi_{tor} \sim \psi_{gun}$, i.e. before flux amplification occurs), the injection rate can be stated as:

$$\dot{K}_{eff} \approx 2L\psi_{gun}\, \dot{I}_{gun} \qquad (8)$$

Where a simple model for L is given in Appendix 3. Equation (8) states that helicity is injected when the current ramps up (much like energy storage in an inductor). In past experiments, the axisymmetric period is brief due to the rapid onset of a kink which has a time-varying inductance until saturation (making it a Type I process). However, under certain conditions a fixed geometry is produced, discussed further in the results section.

IV Results

Several experimental results are categorized here according to the processes that give rise to inductive impedance: either Type I ($\dot{L}$ term dominates) or Type II ($\dot{I}$ term dominates).

IV.1 Type I process: helicity injection with current sheets

By carefully programming the bank to deliver just sufficient current to meet the ejection threshold it is possible to push out a single symmetric current sheet from the gun. Figure 4 shows the evolution of this current sheet in schematic and by use of a sequence of camera images obtained at the mid-plane of the spheromak. As the current sheet is expelled it grows asymmetries (of scale length, $l << R$) and has the appearance of a plasma 'bubble'. The propagation time of the current sheet out of the gun is typically Alfvénic (~few μs). Also shown in Figure 4 are snapshots of the evolution of poloidal flux contour evolution from two-dimensional simulations in SSPX geometry produced by NIMROD simulations, reproducing the phenomenon.

Figure 5 shows a typical time-history of the gun current, voltage and magnetic field at the mid-plane of the flux-conserver as the bubble is pushed out of the gun. Initially the voltage is determined by a fixed inductance and time-varying current ($V_{gun} = L\dot{I}_{gun}$) as current flows in the gun, but when $I_{gun} = I_{thresh}$, the sheet expands from the gun and as it grows in size, L grows to produce a 1600V voltage spike. As the current falls below the ejection threshold, the spheromak disconnects and the voltage falls to ~50V (consistent with a short near the breech of the gun), after which the spheromak decays. By using probes mounted at the edge in the gun, the magnetic flux expelled from the gun is observed to increase with time up to 15mW, then falls quickly to zero in the gap. By

integrating the measured products of voltage and flux, it is possible to show the helicity evolution (Figure 5c). In this particular example, the helicity content of the spheromak is accurately predicted by knowledge of the threshold current alone: for shot 6814 where I_{thresh}=410kA, K= 1.5e-3Wb^2. An edge magnetic coil, calibrated with CORSICA, gives the helicity of the spheromak to be 1.x10^{-3} Wb^2. Note that the measured and predicted helicity contents of the spheromak differ: after the current sheet has been expelled from the gun, the voltage falls to ~300V until $I_{gun} = I_{thresh}$. The measured helicity does not continue to increase after the initial voltage spike, while the integral of $2V_{gun}\psi_{gun}$ shows a continued increase.

IV.2 Type I process: helicity injection by multiple current filaments

Figure 6 shows the current, voltage and magnetic field time-histories for a new operating mode (first reported in [17]) that gives a continued increase of magnetic field strength until the bank runs out of charge (shot #7226). By maintaining $I_{gun} \sim I_{thresh}$, spheromak magnetic field strength grows monotonically and 1.5kV voltage spikes occur with a typical period of 10μs. The voltage spikes raise the mean voltage by more than a factor of two compared with other operating modes, giving the highest sustained rate of injection for SSPX.

The origin of the voltage spikes is explored by use of a number of signal processing techniques. Figure 7 shows the auto spectra for the filtered voltage and field fluctuations, their cross-power spectrum and their coherence. The voltage fluctuations have a much broader spectrum than the magnetic field fluctuations and extend beyond 100kHz. For this analysis, those signals above 100kHz are filtered out as they contribute only fractionally to the total signal. Still, it is significant that the energy in the voltage fluctuations is finite out to and beyond 100kHz, whereas in the magnetic signals, there are virtually no signals with frequency above 50kHz. Further, the voltage fluctuations have large amplitude from low frequency up until 60kHz: more than double the n=1 mode frequency indicating that the rotation of the dough-hook (that generates the n=1 mode signal) is not by itself responsible for voltage fluctuations (voltage fluctuation amplitudes are at minimum at the n=1 mode frequency of 25kHz). This is shown further by a low cross power at all frequencies other than the n=1 mode frequency, and the signals are coherent (gamma>0.6) only at the mode frequency (above 50kHz, coherence becomes meaningless as the magnetic signals fall to insignificant amplitude). The weak coherence is manifest also in the time-delay correlation. Figure 8 shows the correlation function for voltage and magnetic field fluctuations in the gun (between two coils mounted 10cm apart vertically): the magnetic field appears to be well correlated in time with r~1 falling to 0.5 over 40 or so microseconds. There isn't a strong time-correlation between the magnetic field and voltage: r~0.2, but the correlation is finite due to the n=1. In summary, voltage fluctuations at the n=1 mode frequency appear to be coherent with those in the magnetic field spectrum, however these frequencies represent only a small range in frequency over which the energy of the voltage fluctuations is distributed (extending up to and beyond 100kHz) for which signals are incoherent and poorly time-correlated with magnetic field fluctuations.

Certain shots operated with slightly higher gun current show a change of current path and a cessation of magnetic field increase earlier in the time history. Figure 9 shows gun voltage, current, magnetic field, density and fluctuation amplitudes from one of these discharges: note that the magnetic field rolls over at about 2ms, and that the gun voltage changes character from spikey to nearly constant (at ~200V). What makes these discharges different is that the edge toroidal field continues to increase throughout the shot (fig. 9f) indicating a change of current path: current flows increasingly into the flux conserver instead of returning to the gun.

With both the signal analysis and knowledge of the current path, we can build a heuristic model for the origin of the voltage fluctuations (shown in Figure 10). It is the interaction of the out-going and in-bound current paths that leads to discrete reconnection events in the 'nearly stuffed' gun. A mechanism that would entail these properties would be the expulsion of multiple filaments: the helicity that is carried by this filament is additive to the spheromak helicity by further reconnection processes, and so the spheromak field strength grows with time. Further evidence for filament formation in SSPX was presented by Ryutov [27], evidenced by electrode tracks and argued on the basis of an instability arising from the temperature and energy dependences of the particle recycling coefficient.

While the voltage is set as a boundary condition in the NIMROD simulations discussed in this work, it is still possible to simulate the effect of applying a high time-average voltage for an extended period (where in the experiment it is the voltage spikes that raise the average voltage). Simulations of shot #7226 have qualitative and quantitative agreement. With Spitzer temperature-dependent resistivity at finite pressure (peak β_e~6%) and constant thermal conductivities (isotropic χ=100m^2/s), a continued buildup of magnetic energy is observed for pulse times of increasing length but shorter than the resistive decay time (Fig. 11). The initial increase of magnetic energy in the simulation tracks #7226 fairly well. As the plasma heats, the resistivity decreases and the resistive decay time increases, which allows continued increase of the spheromak magnetic fields if the gun voltage is maintained.

IV.3 Type I process: helicity injection by kink formation

Usually in formation shots, there is an initial axisymmetric ballooning of the injector flux which injects helicity and magnetic energy into the flux conserver. If the gun current is programmed to exceed the ejection threshold then an asymmetry soon develops as an MHD kink forms on the geometric axis. This transition is seen in SSPX in most shots and is characterized in the mode analysis shown in Figure 12. The frequency of the n=1 mode is typically around 10-20kHz. Determining the coherence at the n=1 frequency, it is apparent that the mode is globally coherent: the coherence is around unity everywhere. The discrete Fourier analysis reveals a strong n=2 component during the period that the n=1 is present. This is interpreted as a harmonic distortion rather than a true n=2 kink of the toroidal flux. The reason is that the n=2 phase change occurs at twice the rate observed for the n=1.

In NIMROD simulations large *n*=1 MHD perturbations are observed when the plasma is strongly driven by the electrostatic field, shown in Fig. 13. The poloidal magnetic field

perturbation at the outboard mid-plane is $\delta B_z(n=1)/B_z \sim 10\%$; however, the n=1 relative perturbation amplitude is ~25% averaged over the volume in the simulation. Although the toroidally averaged fields in the NIMROD simulation indicate that a mean-field spheromak has formed with flux amplification similar to SSPX shots, the Poincaré surface-of-section plots for tracing the magnetic field lines indicate short, open field lines until the driving voltage has been crowbarred (shorted out), which allows the symmetry-breaking perturbations to resistively decay and closed flux surfaces can then emerge [12][21].

IV.4 Type II Process: helicity injection by pulsing current along a fixed kink

Usually, the vacuum magnetic field is programmed to be radial across the mouth of the gun which can inhibit ejection. The IdL/dt-term, can be minimized by programming a predominately vertical vacuum field, as shown in Figure 1, and is much like that used in the NIMROD simulations. By pulsing the gun current twice along a predominately constant inductance path the magnetic energy increases in a step-wise manner.

Two 450kA current pulses can be produced as shown in Figure 14a by firing each half of the formation bank separately, at 1ms after the sustainment pulse-forming network has fired. Also shown in Figure 14 are: b) resulting gun voltage (peaked twice at around 2kV); c) total magnetic field energy as inferred by a magnetic field coil at the mid-plane calibrated with CORSICA; and, d) plasma line-averaged density measured on a chord through the magnetic axis. Close timing of the two pulses gives an increase of the stored magnetic energy from 18 to 26kJ, after which time, the spheromak decays. By this means, the highest magnetic fields yet observed in SSPX are produced (0.35T at the wall and 0.7T at the geometric axis) and the ratio of the edge field to the injected current is higher by 25% than the previous scaling. CORSICA infers that the increase of the magnetic energy is attributable to an increase of the total current enclosed by the separatrix, i.e. pulsing increases the fraction of current flowing on closed field lines from 210kA to 350kA (an increase of ~70%). During the second pulse, the density is temporarily increased by a factor of two, however it falls rapidly to a level that is consistent with most discharges formed with 450kA. The gray line on Figure 14d shows the attained density after around 100 shots, and by marginally increasing the programmed vacuum field. It is lower compared with the original shots indicating that the large increase of density during the second pulse can be attributed to poor surface conditioning, and the introduction of dense edge plasma.

Figure 15 shows a plot of the gun voltage against the rate of change of injected current for a typical pulsed shot in order to demonstrate the phase relationship between voltage and current for these discharges. The process is identified as inductive by the linear proportionality between V and dI/dt. Note that the absolute magnitudes differ: the first pulse has an inductance of 0.27μH and the second has L~0.2μH – this is discussed below (and also in [26]).

While the n=1 is the dominant mode during the second pulse, the spectrum is quite broad: similar amplitudes out to n=5 indicate a strongly driven configuration, and fluctuation amplitudes are comparable to more usual modes of operating. There is no clear

indication that current sheets are expelled from the gun, instead probes inserted across the mouth of the gun show a very strong asymmetry (100% variations of poloidal and toroidal field there). This is symptomatic of the rotation of the current column that gives rise to the n=1 mode. The asymmetry is not observed at the mid-plane of the spheromak, where calibration errors can explain a 5% systematic asymmetry in the poloidal fields. However, asymmetry is manifest quite strongly at the divertor and lower flux conserver indicating that the injected current path extends from the gun to the divertor. This path is substantiated by the observation of high wall currents (high edge toroidal field), and by camera images that reveal bright asymmetric patches. Camera images do not reveal a large kink at the geometric axis (like those observed by Lindberg), presumably because the impurities burn through to higher ionized states and do not radiate in the visible.

Typically, the temperature profile during the decay of the second pulse is peaked at the magnetic axis at around 120eV. Figure 16 shows a typical temperature profile (at 1.6 ms), just after the second pulse. PTS was scanned throughout the time-history and shows the highest temperatures at around 2ms. At 1.3ms, just before the second pulse, the average core temperature from a number of shots is ~80eV. The local electron beta is typically higher after the second pulse and reaches ~6% in the core.

Increasing the time between pulses results in a quasi-steady sustainment of the configuration. Figure 17 shows the time-histories of the current, voltage, magnetic field and average core electron temperature obtained from 15 similar shots. While the spheromak fields remain finite, the temperature is caused to fall during the pulses due to a large influx of cold plasma, giving also a high density for the second pulse. However, measurement of the beta profile before and after second pulse indicates that confinement recovers after the collapse with the radial profile and magnitude of beta returning to the pre-pulse level.

We used NIMROD to simulate the effects of driving spheromak formation with two voltage pulses. The first voltage pulse forms the spheromak, which is then allowed to decay by crowbarring the driving potential. Closed field lines emerge when the symmetry breaking perturbations are less than a few percent in volume-averaged magnetic energy. The second pulse builds the magnetic energy to a higher level, and there is evidence for a four-fold increase in the volume of closed flux from the first to the second pulse and an increase in the total flux amplification from 4.7 to 5.1 at the times when the driving voltages were crowbarred and from 4.0 to 4.45 in decay when the good flux surfaces shown in Fig. 18 occurred. These increases are not attributable to the decrease in the total dissipation (as the resistivity is not temperature-dependent in this simulation). The driving time for each pulse was 31 ms, and the vertical electric fields near the outer radial boundary of the pillbox were 100 V/m in both pulses. The mass density in this simulation is $\sim 10^4$ greater in the simulation than experiment; both velocities and times scale with the Alfvén speed so this corresponds to ~ 0.3 ms in the experiment. Higher temperatures were achieved after the second pulse than after the first pulse (95 eV at 0.14s vs. 78 eV at 0.056s). The peak plasma electron beta in the simulation was approximately 4% at 0.14s, equivalent to 1.4 ms in the experiment.

V Discussion

Four operating modes have been presented alongside resistive MHD simulations showing qualitative and quantitative agreement. The essence of these operating modes was presented in Section II, namely that the processes that most usefully transfer helicity from the gun to the spheromak are inductive, can be expressed in simple analytic form, and can be harnessed by carefully programming the bank. We find that two new operating modes give a more favorable scaling of the magnetic field with the injected current. These new scalings are shown in Figure 19. We discuss each of the features of these operating modes as follows.

Inductive origin of helicity injection and the role of reconnection

There are several more features of Eq. (7) that warrant consideration: the rate of helicity injection depends on how quickly one is able to push out a current sheet, and it is possible to imagine the production of multiple current sheets. Considering the rate of injection: a less massive sheet would eject more quickly given the same forcing term, and hence one might expect there to be a sensitivity of the injection rate with gas species. This sensitivity has been observed in SSPX, particularly in shots for which there is a high pressure pre-fill. The production of multiple current sheets has also been observed to occur spontaneously in the experiment [28], and some attempts have been made to control the ejection [29]. However, magnetic reconnection is necessary in order for multiple current sheets to be expelled.

The rate of change of inductance can be expressed as in terms of the ultimate inductance of the loop and a time, τ: for the single current sheet, τ is the time taken for the plasmoid to fully disconnect from the gun. *This description requires reconnection: it follows that if the plasmoid does not disconnect, so that another current sheet can form, the helicity of the system is defined explicitly in terms of the inductance (defined by geometry) and the current, for which the spheromak helicity will remain in proportion to* I_{gun}. This proportionality is observed in the experiment for many modes of operating as presented in Figure 19 and so the linear scaling can be understood as the growth to maximum inductance of an ultimately fixed inductance current path, without reconnection, (The pressing question for such a geometry-defined helicity is: what limits the minimum radius of the column? An arbitrarily small column would give an arbitrarily large helicity content, for example.)

Helicity should ramp down as per equation 8, but this is not observed. There are no negative voltage spikes observed in the data. This can be explained somewhat trivially: the flux that is injected remains trapped in the flux conserver and cannot escape, and certainly if it did shift vertically into the gun then it would generate a negative voltage spike. Such vertical instabilities have been observed in SSPX under some unique conditions, but are not evident here.

The steadily building discharges could be described in terms of a ‘Roman Candle’ effect whereby a current filament initiates at some point in the gun and is absorbed by the spheromak at the x-point near to the mouth of the gun. The precise nature of this process remains to be determined, but would have ramifications for galactic magnetic fields,

which still require mechanisms, perhaps of this nature, to generate large flux amplifications.

Scaling of the results to more interesting regimes

Consider first the operating mode in which $I_{gun} \sim I_{thresh}$ for extended periods. As time goes on with the voltage drive fixed in NIMROD the magnetic energy in the simulation surpasses the experiment. The results shown in Fig. 11 suggest that extending the pulse coming from the driving capacitor bank can be beneficial in the experiment.

If the bank could be programmed to deliver a train of pulses, how strong could the magnetic field become? The limiting spheromak magnetic field from multi-pulse injection is determined from the pulse repetition rate, $1/T$, and the spheromak decay rate τ_K, set by resistive losses. Using the helicity balance equation, $dK/dt = 2\psi_g V_g - K/\tau_K$, the limiting helicity content can be found. Defining the helicity input from each pulse $\Delta K_g = \int_t^{t+\delta t} 2\psi_g V_g dt$, where δt is the pulse width of each pulse in the pulse train, and assuming constant τ_K, the limiting helicity content is given by $K_\infty = \Delta K_g \{1 - \exp(-T/\tau_K)\}^{-1}$. This relation balances the input rate from each pulse with the helicity decay between pulses $\Delta K_g \{1 - \exp(-T/\tau_K)\}$ and is for the helicity at the end of each pulse. In this case (with T=300μs and τ_K=1000μs), one would expect $K_\infty = 3.8\Delta K_g$, providing of course that the spheromak dissipation time does not grow with time, in which case there may not actually be a limit to the build-up of helicity [30]. Perhaps surprisingly, we see a doubling of core temperature from the first to the second pulse, which is evidence in favor of such an optimistic projection. However, we are assuming also that ΔK_g does not change on each pulse (which seems not to be the case here: V_{gun} is lower on the second pulse by almost a factor of 2). Thus, a natural experiment to is to add third and even fourth pulses, and monitor the temperature. This is unfortunately not presently possible in the experiment.

Given observed scalings, a simple model has been generated to determine the requirements to reach higher temperatures. The equations used in this model are to be found in Appendix 1. Three scalings based on observation are used: 1) the scaling of temperature with density and field at approximately constant beta [16]; 2) the scaling of density with gun current, in approximately linear form; and 3) the new scalings for the magnetic field with gun current presented here. A Bessel function model is used to infer internal field and current profiles, scaled to a measured edge magnetic field to calculate J in the core and hence the Ohmic heating power and a heating time. This heating time determines the minimum time constraint on the sustainment bank. Hence the size of the sustainment bank can be determined, given also an observed coupling efficiency. We can also calculate the electrode heating, given calorimetry performed on the inner electrode. Given constraints on electrode heating (due to surface melting), and on bank size (due to cost), we are able to determine which operating mode is the most favorable to explore in the future.

As an example of the model, consider the usual SSPX discharges for which we have observed 200eV with 400kA on the formation bank and 200kA on the sustainment. The core temperature is 200eV, edge field is 0.26T, core density is 7e-19m^{-3}, total magnetic energy is 22kJ (in agreement with CORSICA), the coupled formation bank energy needed to achieve this is 150kJ, the ohmic heating time is 0.3ms, and would require a sustainment bank of only 400kJ to maintain stability until 200eV is reached. The simple scaling model shows that for pulsed operation, it would be possible to produce a 1keV spheromak by producing 2 pulses of 1MA. An intermediate step to attaining this would be to install a modular bank that would pulse two pulses of 600kA (or a train of lower current pulses at 400kA). Such a scenario would allow the production of a 0.5T, 500eV spheromak. Such a next step would be necessary for further testing of both the scaling model and the NIMROD simulations.

VI Conclusion

We have demonstrated two new operating modes in SSPX that raise the scaling of the field to injected current significantly above what has been obtained previously. We understand the helicity injection processes that cause this increase in scaling to result from inductive processes in the plasma. Comparison with NIMROD simulations, operated in SSPX-similar parameter space, shows similar features for all of the experimental operating modes. Using a simple scaling model and the understanding gained from scalings observed in the experiment, we are able to predict what bank modifications need to be made in order to produce a spheromak of a given temperature. Further, we indicate that a bank modification should give rise to 500eV spheromaks. This modification is therefore a necessary step towards the production of high temperature plasmas, would give additional scaling information and would serve as a critical test for NIMROD code.

Acknowledgements

The authors would like to acknowledge useful discussions with Dmitri Ryutov and Ken Fowler, and other SSPX team members for keeping the machine operating. An earlier version of this paper was presented as an invited talk at the American Physical Society Division of Plasma Physics meeting, November, 2003. This work was performed under the auspices of the US DoE by the University of California Lawrence Livermore National Lab. under Contract No. W-7405-ENG-48.

Appendices.

Appendix 1 Scaling model

The scaling model entails the following linear scaling relations observed experimentally:

$$T_e(eV) = \frac{\beta(\%)B_p^2(T)}{2\mu_0 n_e(m^{-3})} \quad \text{(A6)}$$

$$B_p(T) = c_1 I_{gun}(A) \quad \text{(A7)}$$

$$n_e(m^{-3}) = c_2 I_{gun}(A) \quad \text{(A8)}$$

$$W_B(J) = \frac{B_p^2(T)}{2\mu_0}\Delta V(m^3) \quad \text{(A9)}$$

$$E_{bank}(J) = W_B(J)/f(\%) \quad \text{(A10)}$$

Where *f* is the empirically-derived efficiency of formation, which is typically small (<10%). The time taken for the plasma to heat to a given temperature is determined by the Ohmic heating power calculated by a Bessel Function approximation for the magnetic fields scaled in proportion to the edge poloidal field B_p, and a Spitzer resistivity:

$$t_{heat}(s) = \frac{k}{c_3}\frac{2}{5}T^{5/2}(eV) \quad \text{(A11)}$$

where $k = en$ and $c_3 = 5.2\times10^{-5} Z_{eff} \mid \lambda \mid J^2 \Delta V$.

Appendix 2 Sharp boundary model

Here we use a simple slab-model to illustrate the ejection threshold. Toroidal flux is generated by axial current flow in the inner electrode and poloidal flux is generated by the injector solenoid. Injector gap distance is Δ, and has a radius *R(>>Δ)*. We assume that the poloidal flux becomes compressed into a channel of width *δ* and length *l*. The toroidal and poloidal fluxes are then written as:

$$\Phi = B_\vartheta(\Delta - 2\delta)l \quad \text{(A12)}$$

$$\Psi = 2\pi R B_p \delta \quad \text{(A13)}$$

By setting the poloidal and toroidal magnetic field components to be equal (magnetic pressure equal at threshold), the magnetic energy can be expressed as:

$$W_B = \frac{\Psi\Phi\Delta}{2\mu_0\delta(\Delta - 2\delta)} \quad \text{(A14)}$$

then by minimizing the magnetic energy with respect to the flux-channel width (dW/dδ=0) one obtains the δ=Δ/4. The threshold for ejection can be written simply as $\lambda_{crit}=4/\Delta$ (where a slab model would give π/Δ). For SSPX, λ_{crit} ~19.1m^{-1}.

Appendix 3 Inductance of a coaxial screw pinch

In the axisymmetric approximation, a column has a magnetic field

$$B = \frac{\mu_0}{r}\int_0^r j(r)dr \quad \text{(A15)}$$

Assume that the current is returning in a cylinder at radius r_m and length L_m. The magnetic energy is thus

$$W = \int \frac{B^2}{2\mu_0} dV = \pi L_m \mu_0 \int_0^{r_m} \frac{dr}{r} \left[\int_0^r jr dr \right]^2 \qquad \text{(A16)}$$

Suppose the column has a radius a, the current is I, and the current density is flat. Then, we can write

$$W = \frac{L_m \mu_0}{4\pi} I^2 \left[\int_0^a \frac{dr}{r} \left(\int_0^r \left(\frac{r}{a} \right)^2 dr \right)^2 \right] \qquad \text{(A17)}$$

$$B_{in} = \frac{\mu_0}{r} \int_0^r Jr dr = \frac{\mu_0 I r}{2\pi a^2}$$

$$B_{out} = \frac{\mu_0 I}{2\pi r}$$

$$W = \int \frac{B^2}{2\mu_0} dV$$

$$= \frac{\pi L_m}{\mu_0} \left[\int_0^a B_{in}^2 r dr \right] + \left[\int_a^b B_{out}^2 r dr \right]$$

$$= \frac{L_m}{16\pi} \mu_0 \left[1 + 4 \ln(b/a) \right] I_{gun}^2$$

$$\textit{and given } W = 1/2 L I^2$$

$$L = \frac{L_m}{8\pi} \mu_0 \left[1 + 4 \ln(b/a) \right]$$

which yields the inductance in terms of the ratio of flux conserver-to-column radius (where the current returns).

[1] T. R. Jarboe Plasma Phys. Controlled Fusion **36** 945 (1994)
[2] H. Alfvén, L. Lindberg, and P. Mitlid J. Nucl. Energy **C1** 116 (1960)
[3] L. Lindberg and C. T. Jacobsen Phys. Fluids S44 (1963), see also L. Lindberg and C. Jacobsen Ap. J. **133** 1043 (1960) and H. Alfvén Ap. J. **133** 1049 (1960)
[4] W. C. Turner, G. C. Goldenbaum, E. H. A. Granneman, J. H. Hammer, C. W. Hartman, D. S. Prono and J. Taska Phys. Fluids **26** 1965 (1983)
[5] T. R. Jarboe, I Henins, A. R. Sherwood, C. W. Barnes and H. W. Hoida Phys. Rev. Lett. **51** 39 (1983)
[6] M. Yamada *Nucl. Fusion* **25** 1327 (1985)
[7] Y. Ono, A. Morita, M. Katsurai and M. Yamada Phys. Fluids B 5 **10** p3691 (1993)
[8] M. R. Brown and P. M. Bellan Phys. Rev. Lett. **64** 2144 (1990)
[9] M. Yamada, Y. Ono, A. Hayakawa, M. Katsurai and F. W. Perkins Phys. Rev. Lett. **65** 721 (1990)
[10] M. Nagata *et al* The 6th Internat. ST Workshop, Nov. 19 - 21, Seattle (1999)
[11] R. C. Duck, P. K. Browning, G. Cunningham, S.J. Gee, A. al-Karkhy, R. Martin and M G Rusbridge Plasma Phys. Controlled Fusion **39** 715 (1997)
[12] C. R. Sovinec, J. M. Finn, and D. del-Castillo-Negrete Phys. Plasmas **8** 475 (2001)
[13] S. A. Colgate, H. Lui and V. Pariev Phys. Plasmas **8** (2001) 2425
[14] A. al-Karkhy, P. K. Browning, G. Cunningham, S. J. Gee, and M. G. Rusbridge Phys. Rev. Lett. **70** 1814 (1993)
[15] H. S. McLean, S. Woodruff, E. B. Hooper, R. H. Bulmer, D. N. Hill, C. Holcomb, J. Moller, B. W. Stallard, R. D. Wood, and Z. Wang Phys. Rev. Lett. **88** 125004 (2002)
[16] B. W. Stallard, D.N. Hill, C. Holcomb Proc. EPS Conf. on Cont. Fusion Plasma Phys. Madeira (2001)
[17] S. Woodruff, D. N. Hill, B. W. Stallard, R. Bulmer, B. Cohen, C. T. Holcomb, E. B. Hooper, H. S. McLean, J. Moller, and R. D. Wood Phys. Rev. Lett. **90** 095001 (2003)
[18] M. G. Rusbridge, S.J. Gee, P. K. Browning, G. Cunningham, R. C. Duck, A. al-Karkhy, R. Martin and J. W. Bradley Plasma Phys. Control. Nuc. Fusion **39** 683 (1997)
[19] C.R. Sovinec, T. A. Gianakon, E. D. Held, S. E. Kruger, D. D. Schnack, and the NIMROD Team Phys. Plasmas **10** 1727 (2003)
[20] C. R. Sovinec, A. H. Glasser, T. A. Gianakon, D. C. Barnes, R. A. Nebel, S. E. Kruger, D. D. Schnack, S. J. Plimpton, A. Tarditi, M. Ch u, and the NIMROD Team, J. Comp. Phys. **195** 355 (2004)
[21] R.H. Cohen, H.L. Berk, B.I. Cohen, T.K. Fowler, E.B. Hooper, L.L. LoDestro, E.C. Morse, L.D. Pearlstein, T.D. Rognlien, D.D. Ryutov, C.R. Sovinec, and S. Woodruff Nucl. Fusion **43**, 1220 (2003).
[22] S. Woodruff Bull. Am. Phys. Soc. (2003)
[23] T. R. Jarboe, F. J. Wysocki, J. C. Fernandez, I. Henins, and G. J. Marklin, Phys. Fluids B **2**, 1342 (1990)
[24] E. B. Hooper, D. Pearlstein, and D. D. Ryutov Nucl. Fusion **39** 863 (1999)
[25] Magnetic Helicity in Space and Laboratory Plasmas, M. R. Brown, R. C. Canfield, A. A. Pevtsov Editors Geophysical Monograph 111, American Geophysical Union, Washington D.C. (1999)
[26] B. W. Stallard *et al* Physics of Plasmas, **10** 2912 (2003)
[27] Ryutov *et al* (2003)
[28] S. Woodruff *et al* Proc. US Japan CT Workshop Feb. (2002)
[29] S. Woodruff *et al* Proc. US Japan CT Workshop Sept. (2002)
[30] T.K. Fowler Fusion Technol. **29** 206 (1996)

FIGURES:

Figure 1. SSPX and major components
Figure 2. SSPX gun circuit
Figure 3. Schematic of the processes that govern the gun voltage in SSPX.
Figure 4. Illustration with fast camera images (courtesy of CALTECH) of the ballooning of a current sheet from the gun.
Figure 5. Time histories of a) gun current, b) spheromak poloidal magnetic field strength at the midplane, c) helicity content, d) gun voltage, e) injected flux and f) helicity decay time.
Figure 6. Steadily building discharge.
Figure 7. Auto power spectra from the filtered gun and field fluctuations, cross-spectrum and coherence
Figure 8. Correlation of magnetic field with gun voltage (solid line) and of two magnetic field coils mounted on the insert-able probes, separated by 10cm vertically. If r is less than 0.5, the signals are said to be weakly correlated..
Figure 9. A steadily building shot that ceased to build part-way through the shot.
Figure 10. Schematic origin of the gun-voltage fluctuations.
Figure 11: NIMROD simulation shows continued magnetic energy buildup with a longer pulse
Figure 12. Mode analysis for formation shot #3099. Note the initial n=0 mode, followed by the n=1 mode (and various harmonics).
Figure 13. (a) Vertical magnetic field Fourier analyzed in angle measured just inside the major radius of the spheromak at the vertical midplane for a simple cylinder simulation as a function of time. (b) Magnetic energy integrated over volume Fourier analyzed in angle as a function of time. Simulation parameters: bicubic finite elements (24 ×24), 6 toroidal Fourier modes, E_0=100V/m, η/μ_0=1/2, $\tau_A \sim 10^{-5}$s, $\tau_r \sim 8\times10^{-2}$s, $n = 10^{21}$m^{-3}, $m_{ion}=10^3 m_h$, $\chi_{\|} = 10^3$ m^2/s, $\chi_{\perp} = 10$ m^2/s, $v_A=2\times10^6$ m/s
Figure 14. Results of double pulsed operation with the n=1 mode.
Figure 15. V vs dI/dt for pulsed build-up for shot 11170
Figure 16. Temperature profiles for pulse build-up
Figure 17. From shot MF+5#10223: a) gun current; b) gun voltage; c) edge poloidal field at the midplane; d) density from chord through the magnetic axis; and, e) average core temperature from a series of nominally identical shots.
Figure 18. NIMROD simulations of double pulsed operations.
Figure 19. Scaling of B vs I for operation with n=1 mode (solid line), operation at the ejection threshold (empty circles) and double pulsed operation (solid circles).

Parameter	**SSPX**
Major Radius (m)	0.5
Minor Radius (m)	0.2
Plasma Current (kA)	400
Magnetic field B_0(T)	0.5
Pulse Length, (ms)	3.5
Density, n ($10^{19}m^{-3}$)	2-10
Electron Temperature, T_e (eV)	200
Ion Temperature, T_i (eV)	<600
Beta, $=2\mu_0\langle p\rangle/B(a)^2$	0.1

Table 1. Typical parameters for SSPX

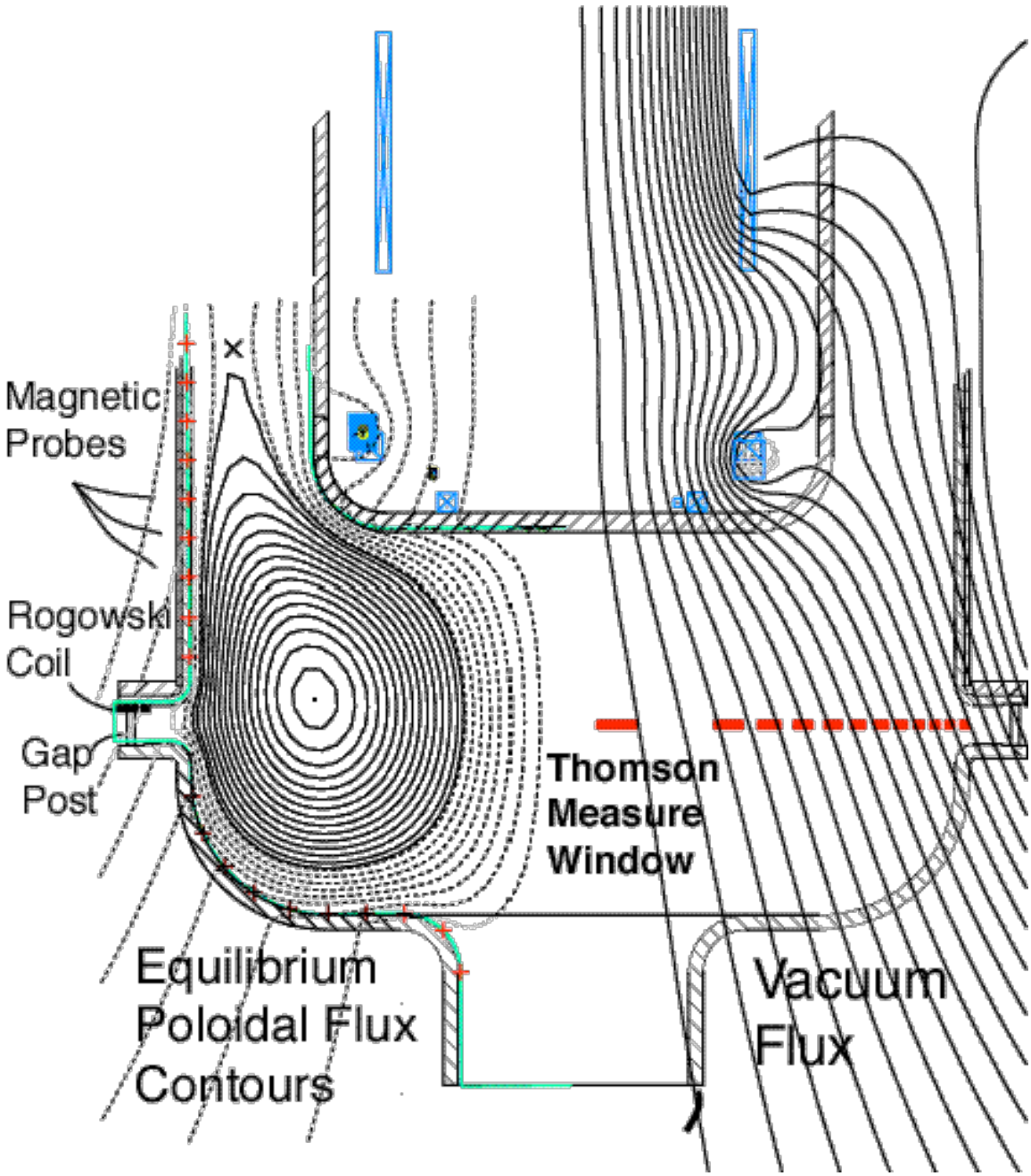

Figure 1. SSPX and major components, showing vacuum field configuration (right) and typical CORSICA-generated equilibrium poloidal flux contours (left).

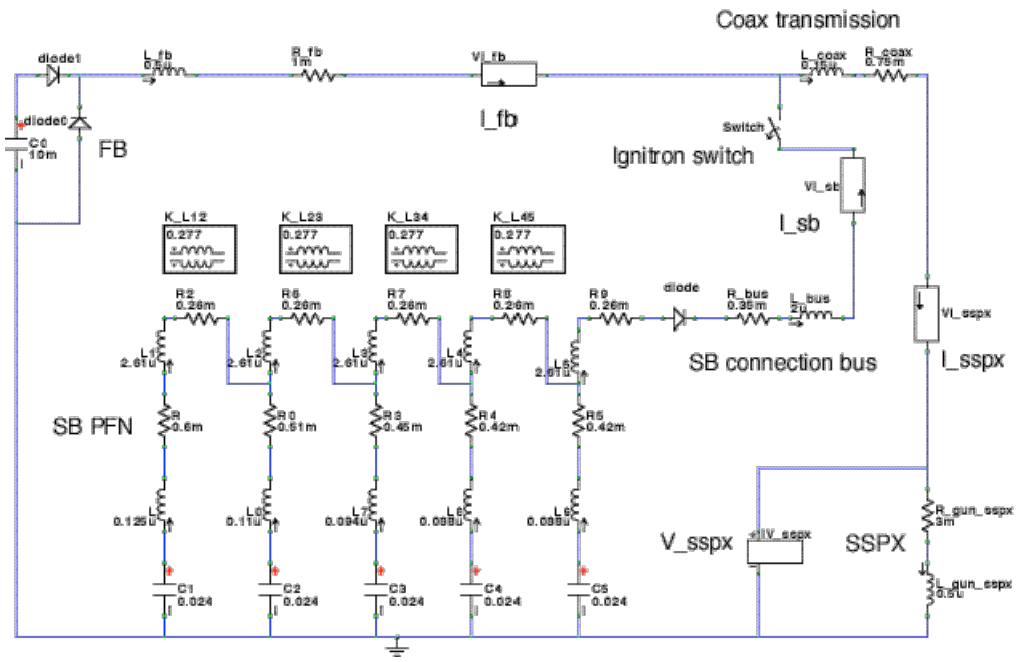

Figure 2. SSPX bank circuit showing both LRC formation section and Pulse Forming Network section of the sustainment bank.

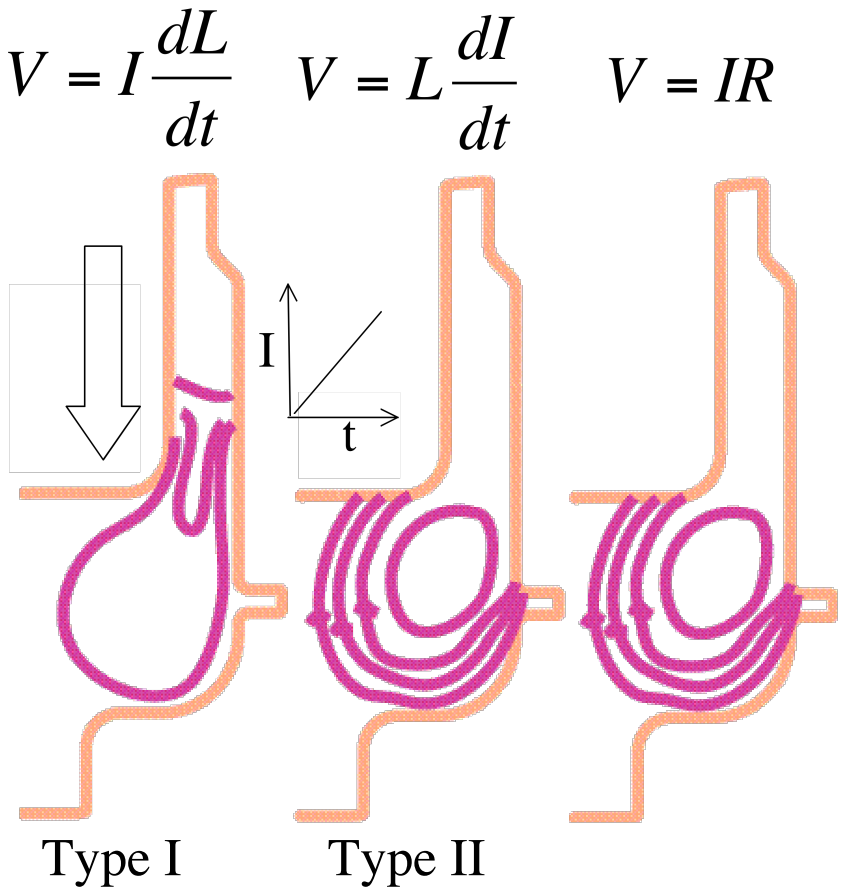

Figure 3. Schematic origin of the processes that govern the gun voltage, illustrating type I and type II inductive processes. In Type I processes, a current sheet is shown at three successive times. In Type II processes, the current increases with time in a fixed geometry and thus with constant inductance.

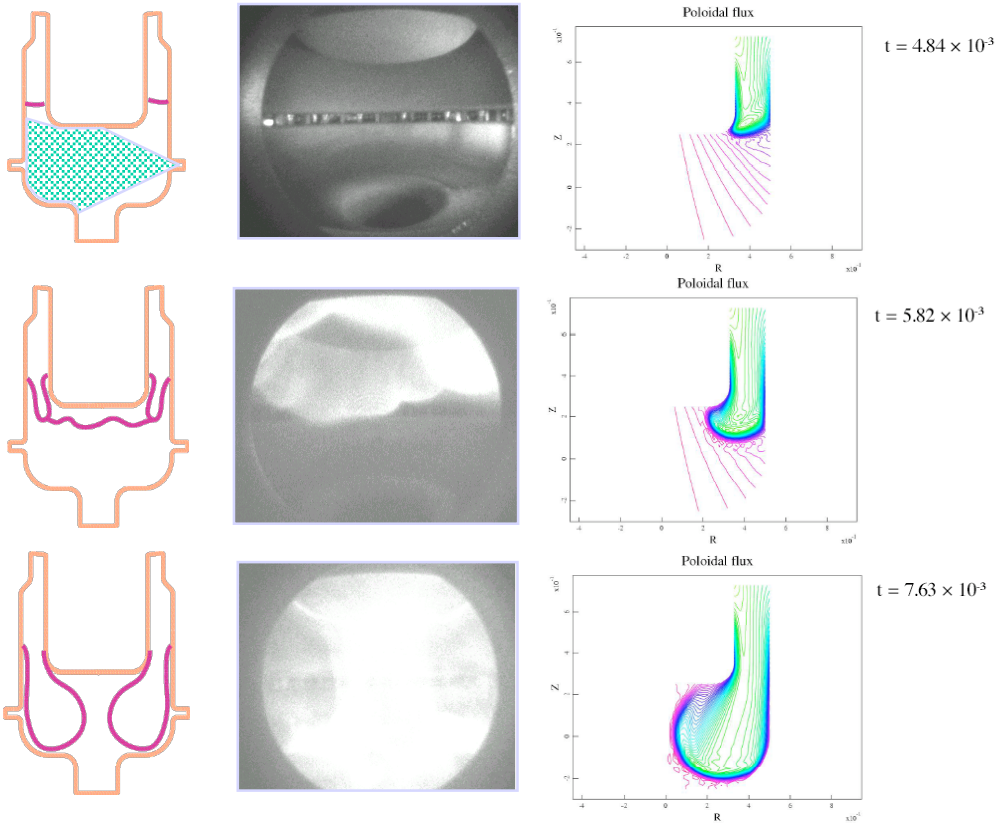

Figure 4. Single pulsed formation – sketch, camera images and NIMROD simulation showing a current sheet being expelled from the gun in SSPX-like geometry.

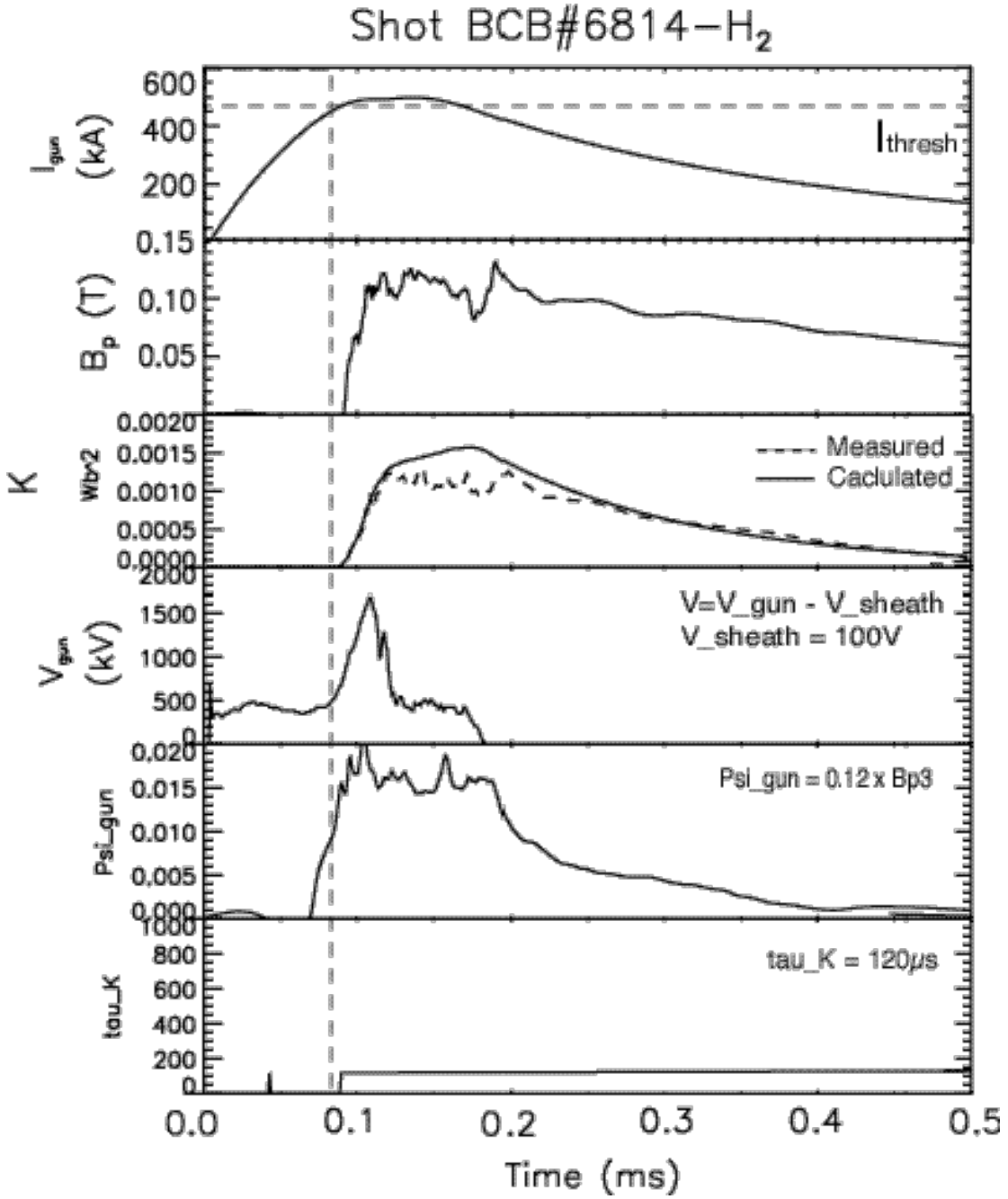

Figure 5. Time histories of a) gun current, b) spheromak poloidal magnetic field strength at the midplane, c) helicity content, d) gun voltage, e) injected flux and f) helicity decay time. The calculated helicity is found by integrating the product of gun flux and voltage; the measured helicity is inferred from the magnetic field at the flux-conserver midplane.

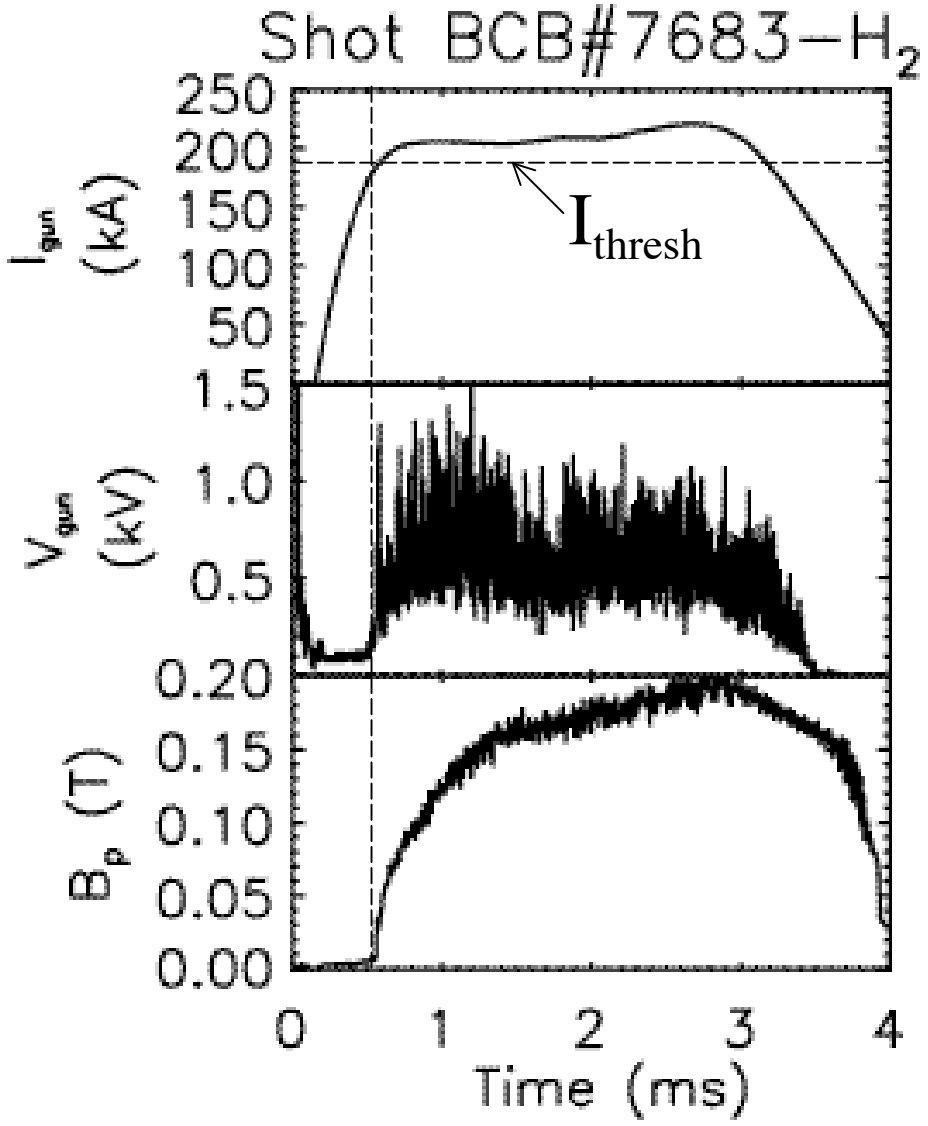

Figure 6. Steadily building discharge: a) gun current; gun voltage; and, c) edge poloidal magnetic field strength at the midplane.

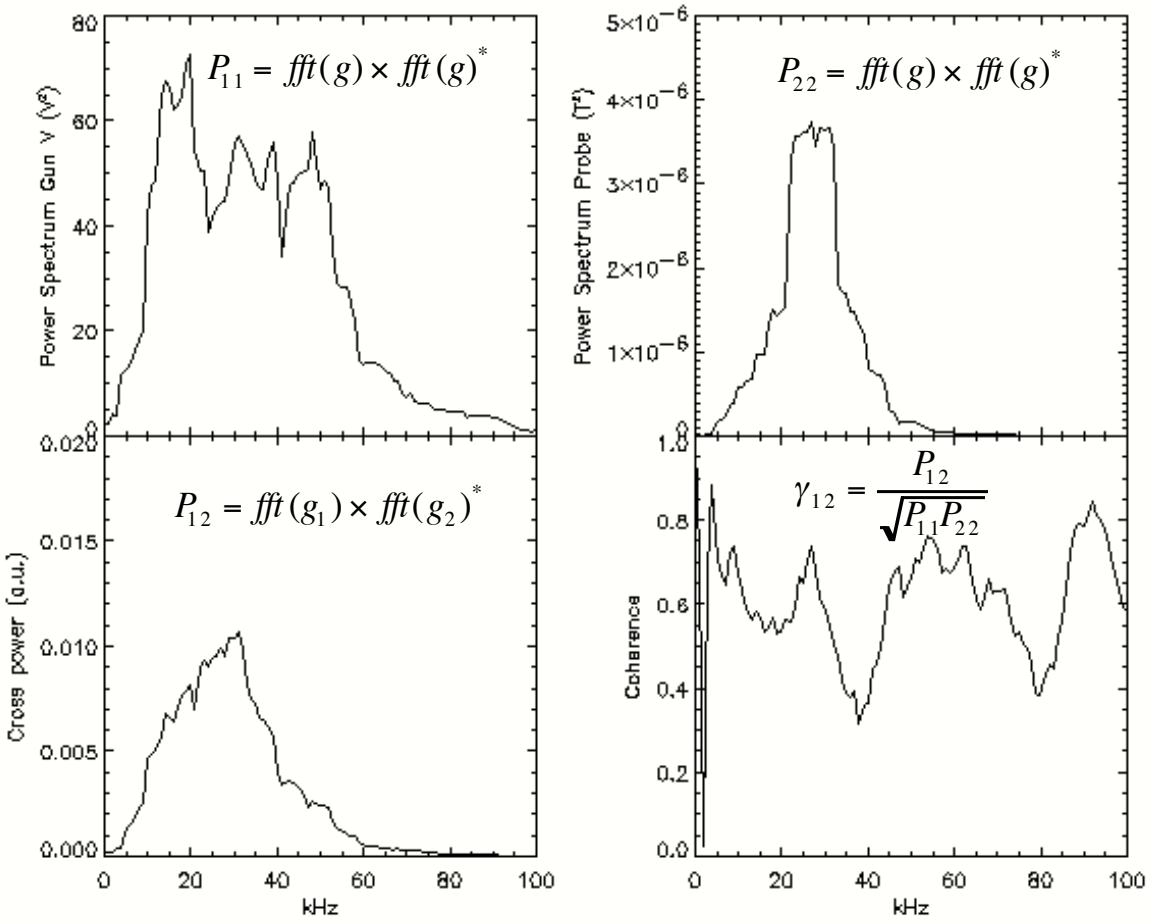

Figure 7. a) Auto power spectra from the filtered gun and b) field fluctuations, c) cross-spectrum and d) coherence.

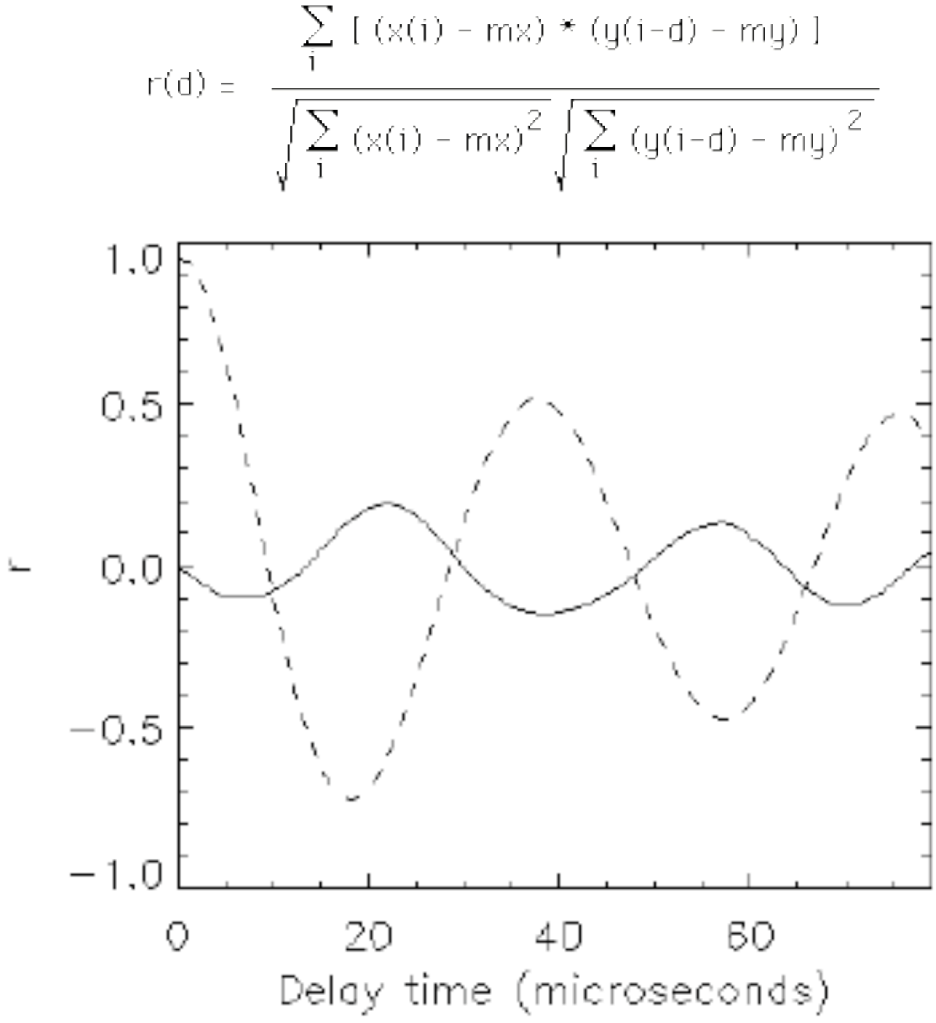

Figure 8. Correlation of magnetic field with gun voltage (solid line) and of two magnetic field coils mounted on the insert-able probes, separated by 10cm vertically. If *r* is less than 0.5, the signals are said to be weakly correlated.

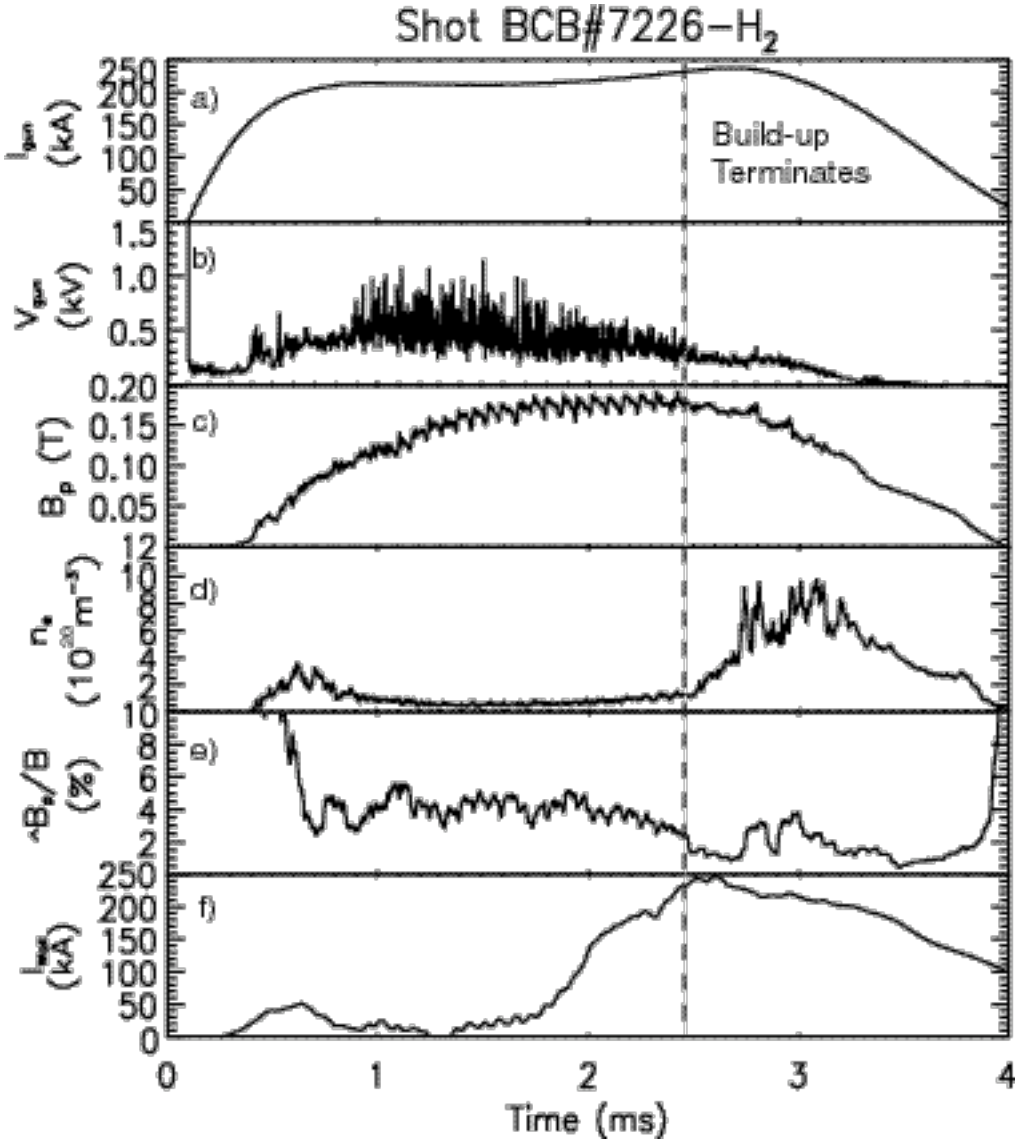

Figure 9. A steadily building shot that ceased to build part-way through the shot.

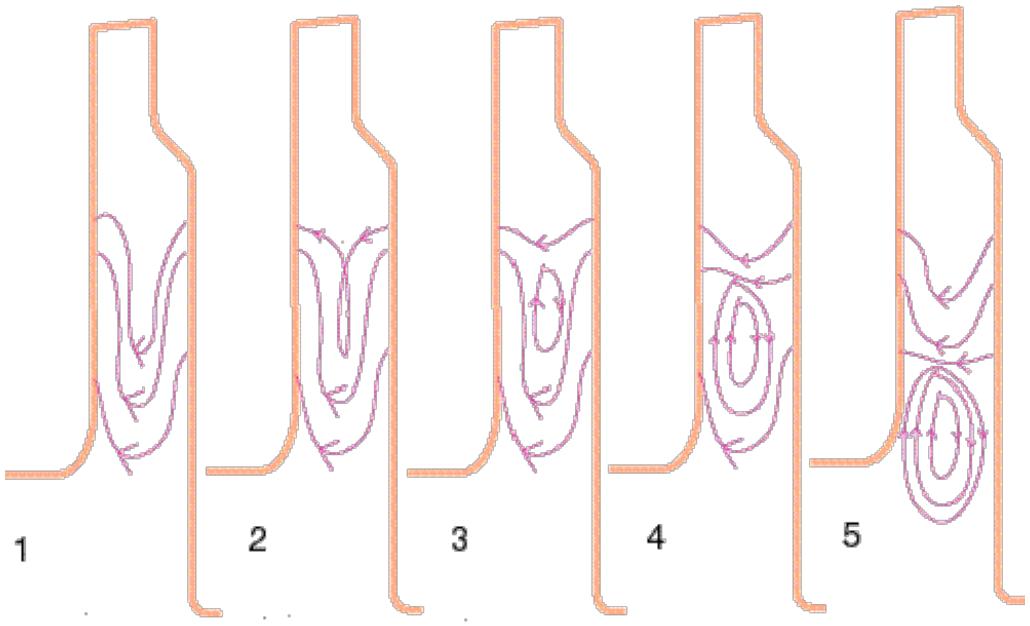

Figure 10. Schematic origin of the gun-voltage fluctuations. A stuffed gun has a current channel that exits and returns to the gun (1); inbound and outbound channels reconnect to form an asymmetric plasmoid (2-4); which is expelled from the gun (5).

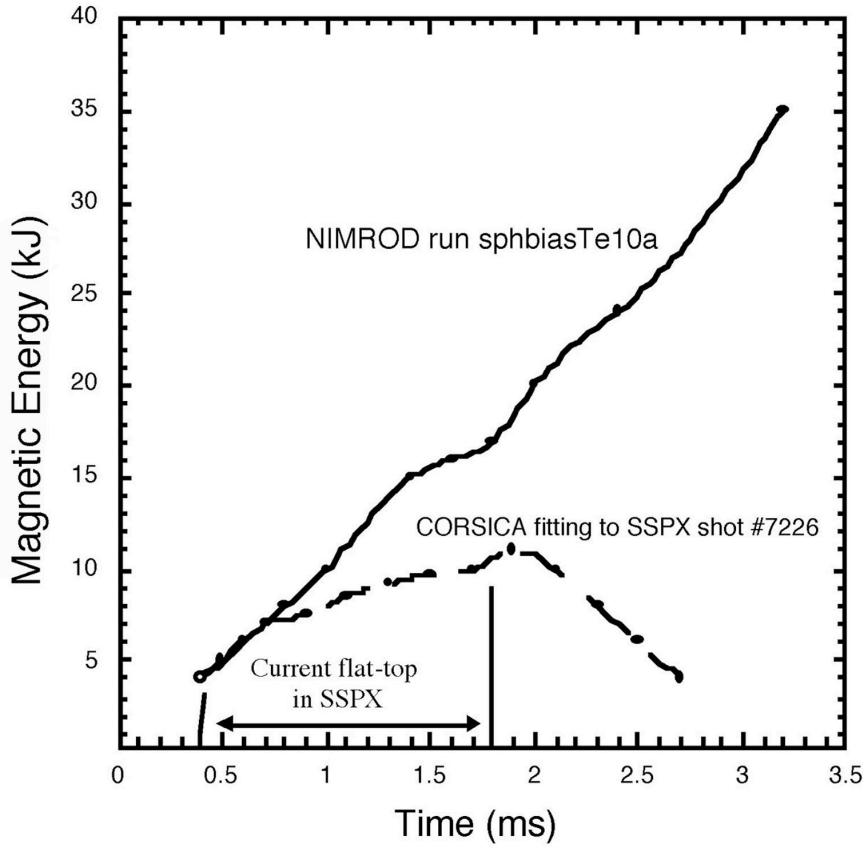

Figure 11. NIMROD simulation at constant gun voltage shows continued magnetic energy buildup with a longer pulse

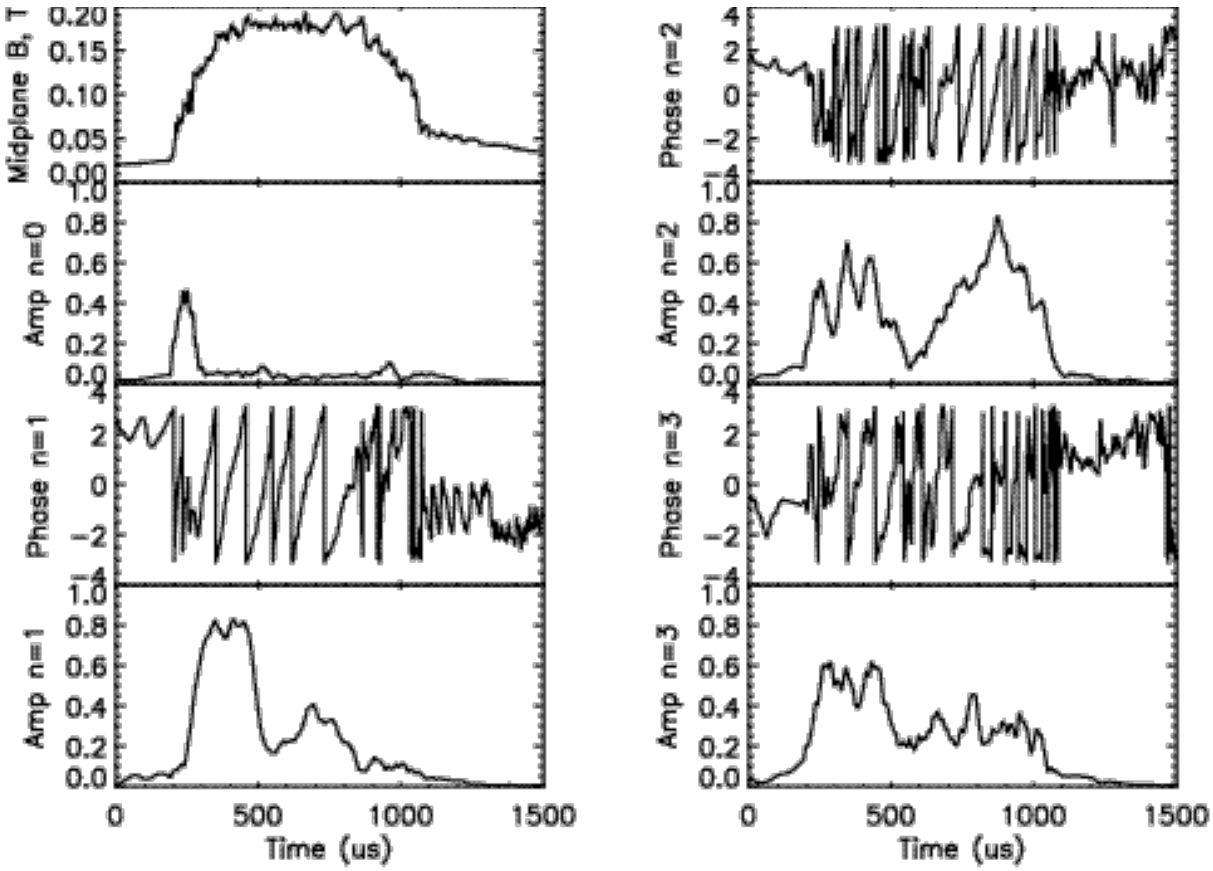

Figure 12. Mode analysis for formation shot #3099. Note the initial n=0 mode, followed by the n=1 mode (and various harmonics).

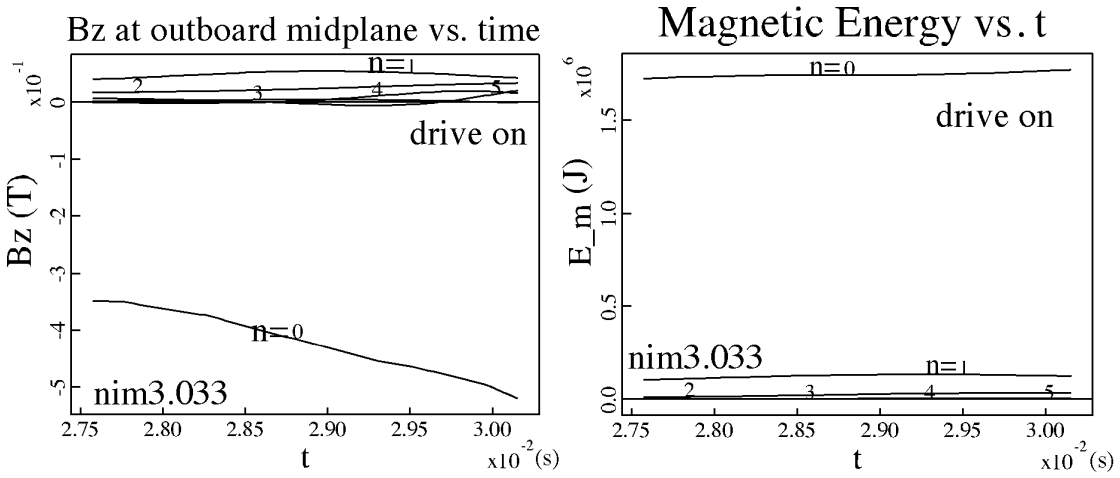

Figure 13. Results of NIMROD simulation: (a) Vertical magnetic field Fourier analyzed in angle measured just inside the major radius of the spheromak at the vertical midplane for a simple cylinder simulation as a function of time. (b) Magnetic energy integrated over volume Fourier analyzed in angle as a function of time. Simulation parameters: bicubic finite elements (24 ×24), 6 toroidal Fourier modes, E_0=100V/m, η/μ_0=1/2, τ_A~10^{-5}s, τ_r~8×10^{-2}s, n = 10^{21}m^{-3}, m_{ion}=$10^3 m_h$, $\chi_{\parallel}$ = 10m^2/s, $\chi_{\perp}$ = 1m^2/s, v_A=2×10^6 m/s.

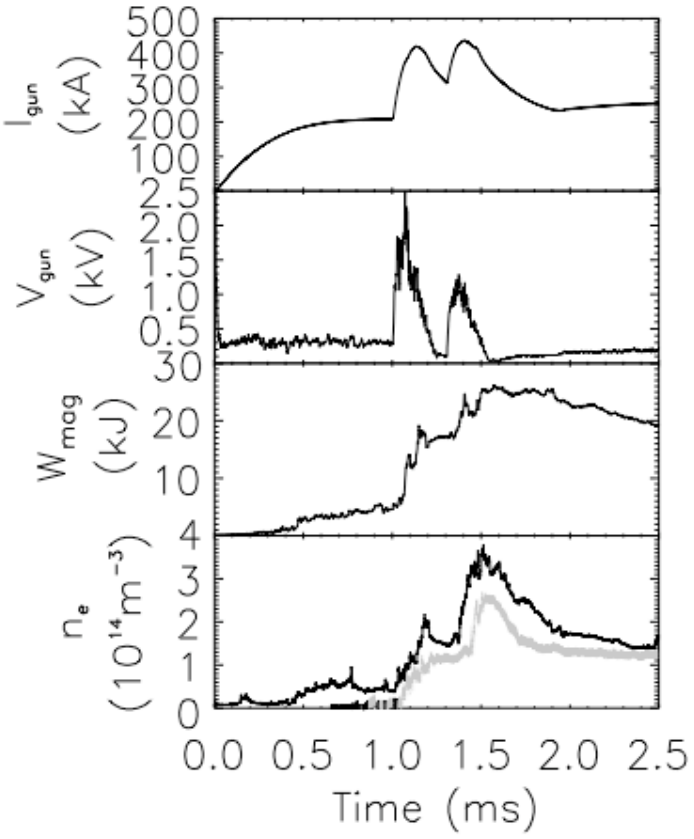

Figure 14. Results of double pulsed operation with the n=1 mode.

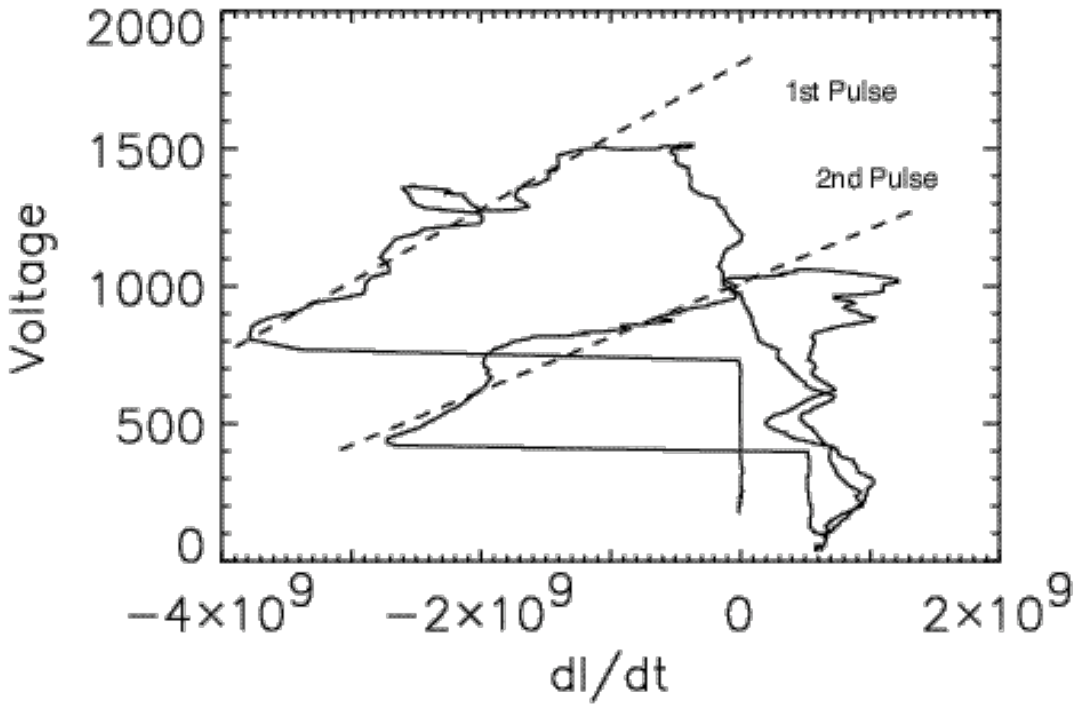

Figure 15. V vs dI/dt for pulsed build-up for shot 11170

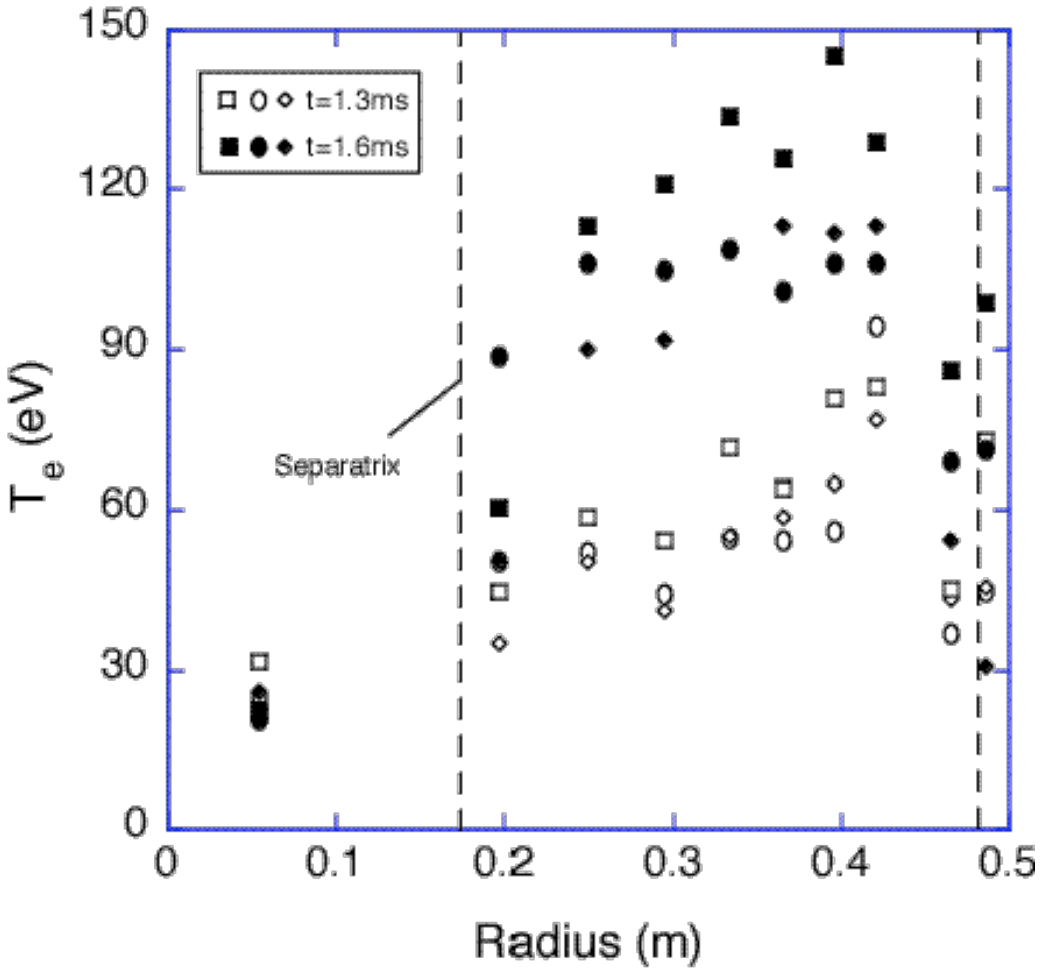

Figure 16. Temperature profiles for pulsed build-up. Two times are shown for three similar shots.

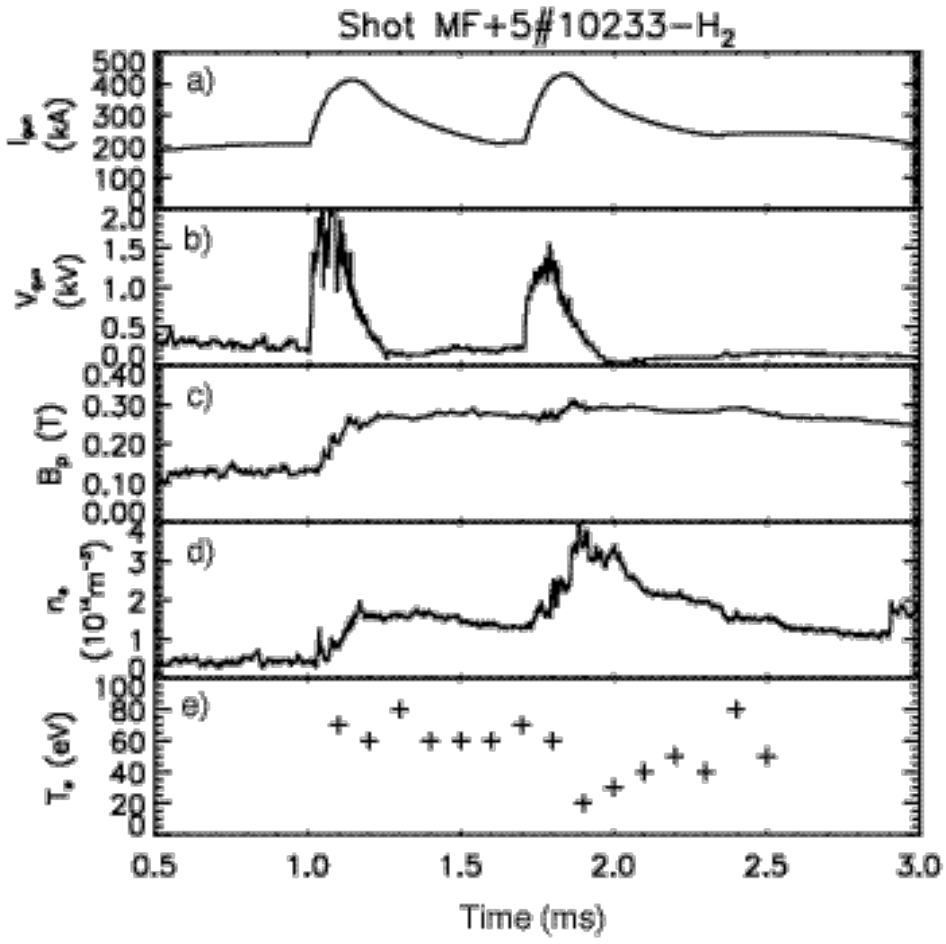

Figure 17. From shot MF+5#10223: a) gun current; b) gun voltage; c) edge poloidal field at the midplane; d) density from chord through the magnetic axis; and, e) average core temperature from a series of nominally identical shots.

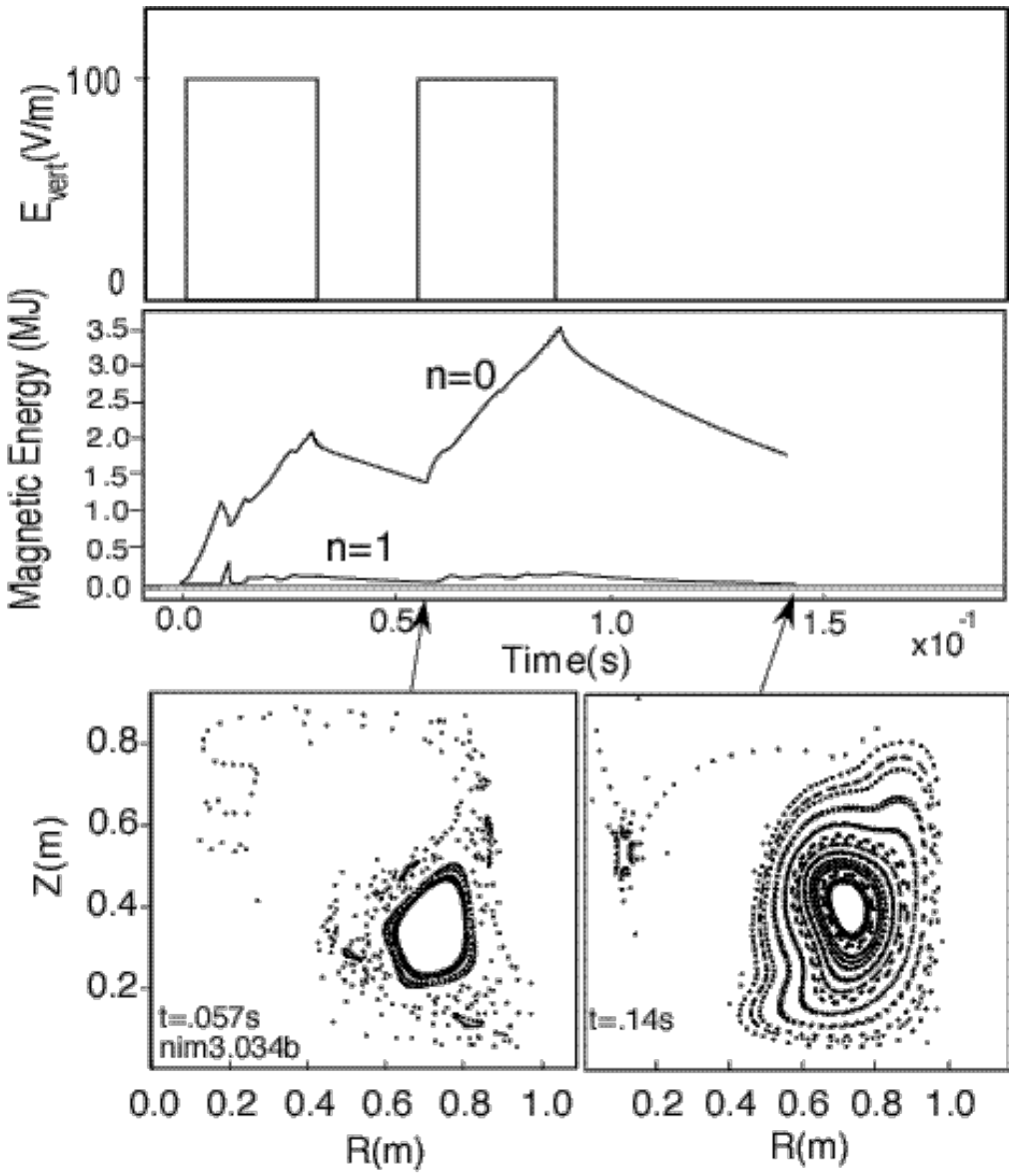

Figure 18. NIMROD simulations of double pulsed operations.

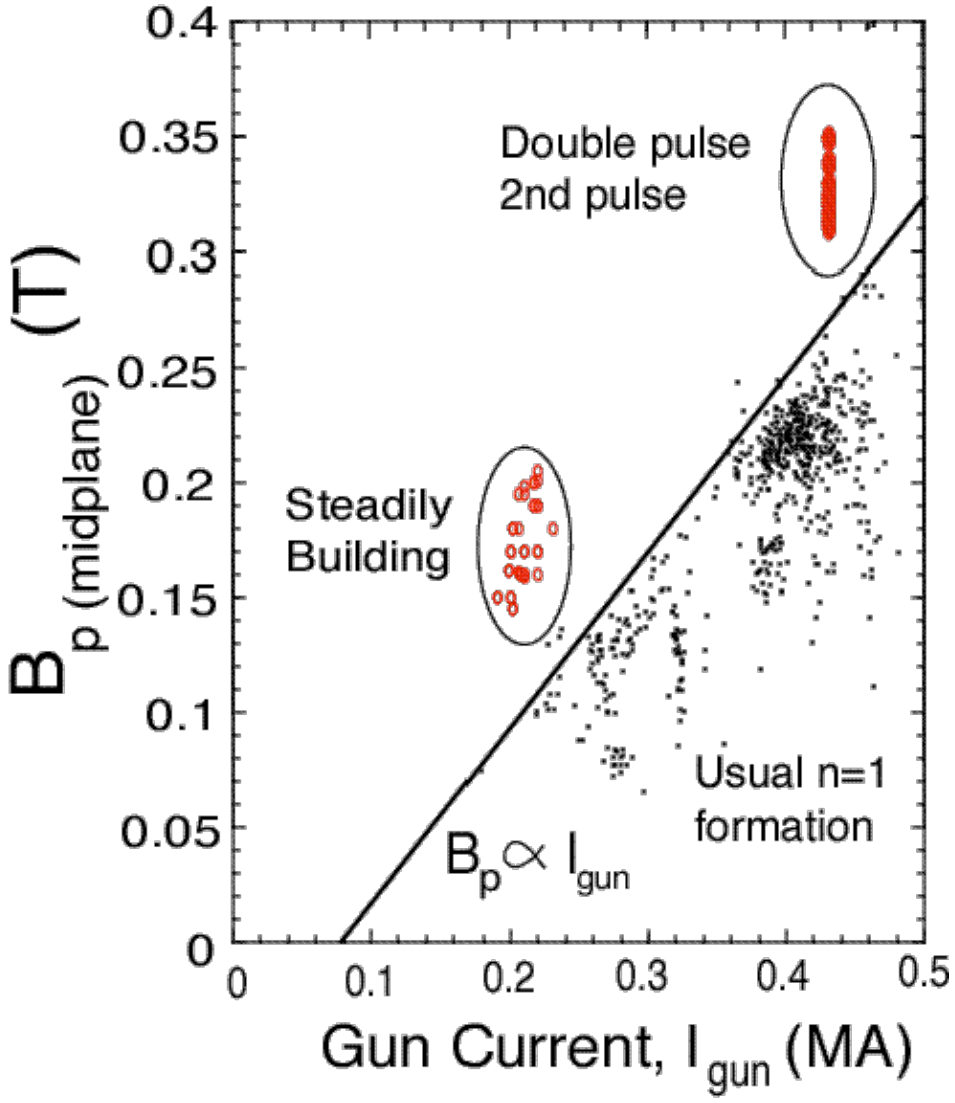

Figure 19. Scaling of B vs I for operation with n=1 mode (solid line), operation at the ejection threshold (empty circles) and double pulsed operation (solid circles).